Catena 221 (2023) 106752

Contents lists available at ScienceDirect

Catena

journal homepage: www.elsevier.com/locate/catena

Multiple forcing on Late Miocene East Asian Summer Monsoon Precipitation Variability in NE Tibetan Plateau

Zhengchuang Hui[a,*], Jia Liu[b,*], Manuel Chevalier[c], Xiao Wei[a], Peng Chen[a], Jun Zhang[d], Tingjiang Peng[d], Xuewen Zhou[a]

[a] College of Geography and Environmental Science, Henan Key Laboratory of Earth System Observation and Modeling, National Demonstration Center for Environmental and Planning, Henan University, Kaifeng 475004, China
[b] CAS Key Laboratory of Tropical Forest Ecology, Xishuangbanna Tropical Botanical Garden, Chinese Academy of Sciences, Mengla 666303, China
[c] Institute of Geosciences, Sect. Meteorology, Rheinische Friedrich – Wilhelms - Universität Bonn, Auf dem Hügel 20, 53121 Bonn, Germany
[d] Key Laboratory of Western China's Environmental Systems (Ministry of Education) College of Earth and Environmental Sciences, Lanzhou University, Lanzhou 730000, China

ARTICLE INFO

Keywords:
Pollen
Probability density function
Global cooling, Tectonic uplift
Eccentricity forcing

ABSTRACT

Understanding how the East Asian Summer Monsoon (EASM) evolves at different time scales affords a valuable opportunity to reveal the interactions between the hydrosphere, land, oceans and atmosphere. However, the pre-Quaternary evolutionary history and the driving forces that controlled its variability in response to different boundary conditions remain enigmatic. Here, we focus on the late Miocene (~10.8 to 6.3 Ma) – a period of profound climatic and topographic changes in Asia – and present a quantitative reconstruction of EASM precipitation using the probabilistic CREST (Climate Reconstruction Software) method with a high temporal resolution pollen record from the Tianshui Basin in NE Tibetan Plateau (TP). Our new EASM precipitation record shows a slowly decreasing long-term trend during the period of ~ 10.8–7.6 Ma, which was followed by a strengthening period from ~ 7.6 to 6.3 Ma with a large amplitude of precipitation variability. We argue the decrease and increase periods of EASM precipitation were primarily response to late Miocene global cooling and TP uplift after ~ 8 Ma, respectively. These results are supported by existing climate model simulations, wherein both global climate and paleotopography play key roles in regulating the long-term evolution of late Miocene EASM. On orbital time scales, the precipitation time series exhibit a dominant ~ 410 kyr eccentricity periodicity, with lower (higher) values intervals corresponding to eccentricity minima (maximum). The synchronous phase of the precipitation and eccentricity records indicate that the eccentricity exerts a dominant influence on the EASM precipitation cycles via its modulation of the precessional amplitude, and the period expansion and contraction of Antarctic ice sheet (AIS) also probably play an important role during that time. Our quantitative late Miocene EASM precipitation records provide new insight into late Miocene EASM precipitation evolution and its relation with global climate, paleotopography, and cryosphere.

1. Introduction

Changes in the monsoon system reflect the interactions of the Earth's surface systems, including the lithosphere, hydrosphere, atmosphere, cryosphere, and biosphere, and are the result and link of interactions between ocean, continent, and air under the background of solar radiation variability (An, 2000; Wu et al., 1997). As such, deciphering the monsoon evolution history can provide critical information to better understand the processes and mechanisms of interactions between these different spheres. The East Asian Monsoon is the principal and direct factor that controls climate variations in East Asia (An, 2000; An et al., 2015) and consists of two sub-systems, the summer and winter monsoon systems (Wen et al., 2016; Webster, 1998). The former delivers heat and moisture from the low-latitude oceans to the Asian interior during the boreal summer months. Conversely, the latter transports cold and dry air from the mid–high latitude Eurasian towards the low-latitude oceans during the boreal winter months. The precipitation brought by the East Asian summer monsoon (EASM) influences almost all aspects of hydrology, economic and societal activities in East Asia, where roughly one-third of the world's population lives (Webster et al., 1998; Clift and

* Corresponding authors.
E-mail addresses: huizhch@henu.edu.cn (Z. Hui), liujia@xtbg.ac.cn (J. Liu).

https://doi.org/10.1016/j.catena.2022.106752
Received 24 June 2022; Received in revised form 4 October 2022; Accepted 31 October 2022
Available online 10 November 2022

Plumb, 2008). Consequently, the research on the evolution of EASM precipitation over different timescales has attracted much attention from geographers, paleobiologists, climatologists, and geologists (e.g., Wang et al., 2019a and b; Ren et al., 2020; Piao et al., 2020; Wang et al., 2020; Zhao et al., 2020; Hui et al., 2021), to quantitatively constrain its driving forces from different research fields of geoscience, and to provide further insight about the future of the EASM precipitation in response to higher temperature/warming scenarios.

Although within the global Cenozoic cooling trend, the late Miocene (~11.6 to 5.3 Ma) still represents a geologically recent interval of significantly warmer climate than today's. It was characterized by profound changes in climate and environment, ecosystems, cryosphere, and regional topographies (Bradshaw et al., 2012; Li et al., 2014; Hui et al., 2011; An et al., 2001; Zachos et al., 2001; Herbert et al., 2016), with for example, the climate transition from a warmer mode with a less stable or ephemeral Antarctic ice sheet (AIS) to a colder, more permanently iced mode (Zachos et al., 2001), the rapid rise of the Tibetan plateau (TP) and the mammal faunas' turnovers occurred (Li et al., 2014), and the seasonality in Asia enhanced (e.g. 'wet-gets-wetter' in southeast Asia and 'dry-gets-drier' in Asian interior, Ao et al., 2021). This period, therefore, encompasses several major global and regional transformations and thus offers an ideal time window to investigate how the EASM precipitation responded to changing boundary conditions, such as ice sheet, topography, and global temperature variations in a warmer-than-modern environment (Holbourn et al., 2021; Nie et al., 2017; Wang et al., 2019a; Ao et al., 2016).

The late Oligocene or early Miocene onset of the modern EASM monsoon system has been generally accepted (Sun and Wang, 2005; Qiang et al., 2011; Fang et al., 2020). However, the detailed evolution of the EASM since the Miocene remains an issue of intense debate, especially for the late Miocene period. The chemical index of alteration (CIA) in the marine sediments from the South China Sea (SCS) and phytolith assemblages and grain size in the terrestrial sediments from Weihe Basin in northern China show that a gradually weakening pattern of the EASM intensity during the late Miocene at tectonic time scales (Wan et al., 2010; Wei et al., 2006; Wang et al., 2019a; Clift, 2020; Clift et al., 2014). In contrast, the ratios of frequency-dependent magnetic susceptibility (χ_{fd}) to hard isothermal remanent magnetization (HIRM) in lacustrine to braided reiver depositions from the Qaidam Basin indicate that the EASM enhanced during ~ 11–7 Ma and gradually weakened after ~ 7 Ma (Ren et al., 2020; Nie et al., 2020), whereas, the magnetic susceptibility and citrate-bicarbonate-dithionite (CBD) records in red clay sediments from Tianshui Basin in Northern China show a broadly reverse trend, that is, a weakened period of ~ 11–8 Ma, and strengthened again after ~ 8 Ma (Qiang et al., 2011; Sun et al., 2015; Zhao et al., 2020). These different EASM evolution histories led to various views concerning its main driving forces and their relative influence, including the global cooling trend, the Antarctic ice volume and CO_2 variations, and the uplift of the TP (Holbourn et al., 2021; Wan et al., 2010; Zhao et al., 2020; Nie et al., 2020; Ren et al., 2020; Ao et al., 2016; An et al., 2001).

Miocene records of EASM variations at orbital timescale are scarce compared to the Quaternary period, and those that exist are not compatible. The lightness in sediments from Guide Basin, χ_{fd}/HIRM from Qaidam Basin, and the susceptibility and the ratio of rubidium (Rb) to strontium (Sr) records from the Tianshui Basin in NE TP show that EASM intensity variations were paced by dominant eccentricity cycles (~100 kyr) during the middle to late Miocene (Nie et al., 2017; Wang et al., 2017, 2019b). In contrast, the lithological variations of the Yanwan (YW) section in the Tianshui basin show dominant obliquity (~41 kyr) cycles during ~ 13.7–13.2 Ma (Fig. 1; Wang et al., 2019b; Heitmann et al., 2017). In addition, the palynological record from the Yaodian (YD) section indicates a long-term stepwise drying trend, which is clearly different from the susceptibility and Rb/Sr records that only

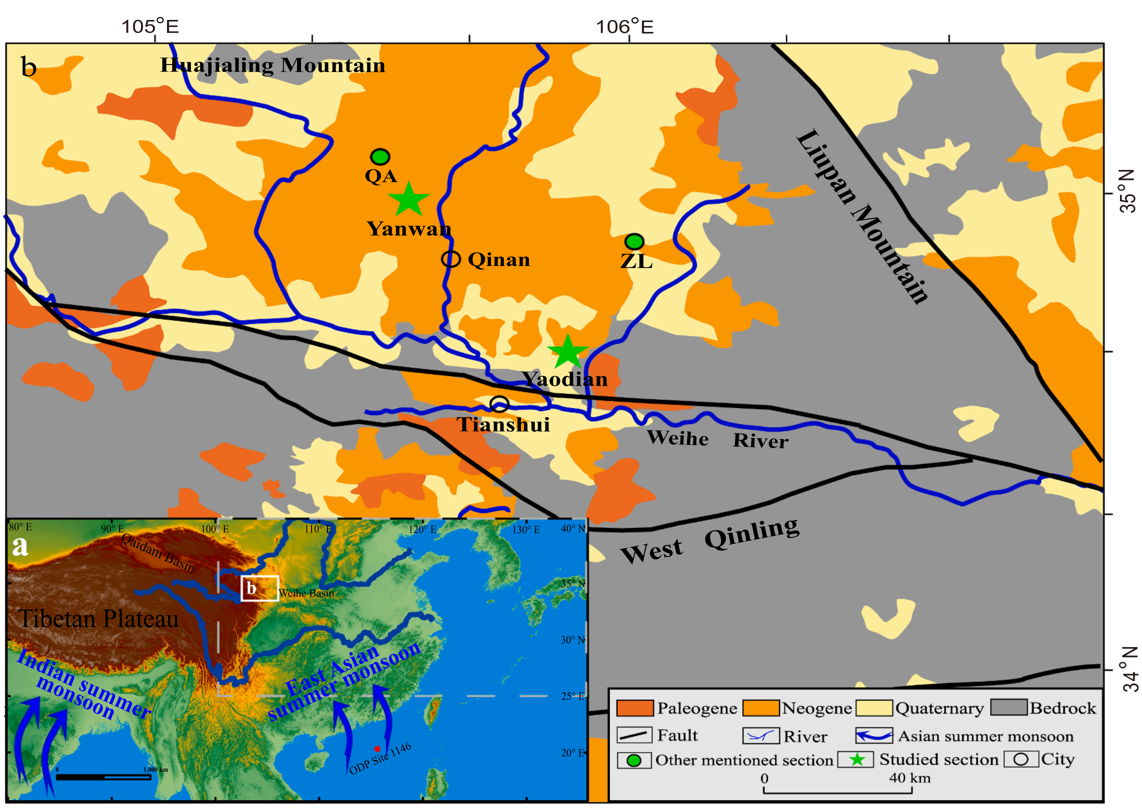

Fig. 1. Geographic and geological setting of study area (modified from Hui et al., 2021). (a) Location and atmospheric circulation patterns of the Tianshui Basin. (b) Geological setting of Tianshui basin, and other mentioned sections in the text. The grey dashed rectangle indicates the calibration region for quantitative reconstruction. The green stars show the studied sections and the green dots show the mentioned sections in the text. YW: Yanwan section, YD: Yaodian section, QA: Qin'an, ZL: Zhuanglang core. (For interpretation of the references to color in this figure legend, the reader is referred to the web version of this article.)

exhibited orbital cycles through time (Liu et al., 2016; Wang et al., 2019b). In summary, the evolution process and driving forces of EASM during the Miocene over tectonic-to-orbital timescales are still extensively controversial. This probably partly stems from the vast area of the monsoonal region and the complexity of the driving forces of the EASM intensity evolution, and the different proxies used for EASM history reconstructions.

In this study, we used the pollen record of the YD section of the Tianshui Basin in the NE TP (Liu et al., 2016) as the basis to quantitatively reconstruct the precipitation during the wettest quarter (PWetQ) – which we consider to be a reliable proxy of the EASM intensity – using the CREST (Climate Reconstruction Software) technique (Chevalier et al., 2014) and coupled with the CREST-specific calibration dataset derived from the Global Biodiversity Information Facility (GBIF) database by (Chevalier, 2019). We integrate this new reconstruction with previously published EASM records from the YW section of the same basin (Hui et al., 2021) to derive a relatively high-resolution quantitative time series uncovering the history of EASM precipitation during the late Miocene. This quantitative record, combined with existing regional and global late Miocene climate records, enables us to investigate the driving mechanisms of late Miocene EASM precipitation over tectonic-to-orbital timescales.

2. General setting

The Tianshui Basin is a sub-basin of the large intermountain Longzhong Basin located on the NE TP. It is bounded by the Huajialing Mountains to the northwest, the Liupan Mountains to the east, and the West Qinling Mountains to the south (Fig. 1A and B). The Neogene sediments named the "Gansu Group" are widely distributed across the Tianshui Basin and lie unconformably on top of the Paleogene sequence called the "Guyuan Group". In most areas, it is capped by Quaternary loess (Li et al., 2006; Zhai and Cai, 1984). According to field observations and previous research work in this region, the Neogene stratigraphy mainly comprises sandstone beds, brown–red mudstone, and calcareous gray-green mudstones distributed along both sides of the rivers (Zhang et al., 2013a). They are interpreted as fluvial channel deposits, floodplain deposits, and lacustrine deposits, respectively (Li et al., 2006; Alonso-Zarza et al., 2009).

Today, the region's climate is mainly controlled by the EASM and is characterized by hot-humid summers and cold-dry winters. The mean annual temperature (MAT) and mean annual precipitation (MAP) of this region are ~ 10 °C and ~ 500 mm, respectively, with most of the precipitation falling from June to September (PWetQ ~ 300 mm) (Liu et al., 2016). Synthesis studies demonstrate that the EASM has influenced the climate in this region since the early Miocene (Miao et al., 2016; Sun and Wang, 2005), confirming that the Tianshui Basin has the potential capacity to capture the variability of the EASM at these timescales.

The modern natural vegetation is warm-temperate forest-grasslands, dominated by the herbaceous species *Bothriochloa ischaemum*, *Artemisia giraldii*, and *Stipa bungeana*. Warm grasslands, consisting mainly of *Arundinella hirta*, *Spodiopogon sibiricus*, and *Themeda triandran* occupy valleys lower than ~ 1000 m a.s.l.. Shrubs (such as *Sophora viciifolia* and *Ostryopsis davidiana*) lie on the hills, and trees (such as *Quercus liaotungensis*, *Pinus tabulaeformis* and, *Platycladus orientalis*) grow in the mountains (Huang, 1997).

3. Materials and methods

3.1. Lithology, depositional environments, and chronology of the YD section

The studied YD section (105°55′ E, 34°38′ N) lies northeast of the city of Tianshui, on the west bank of the Niutou River, which is a small tributary of the Weihe River (Fig. 1B). This Neogene section is capped by loess and lies unconformably on top of the Paleogene Guyuan Group. Based on detailed lithologic properties, it was divided into three formations from bottom to top: the Ganquan, Yaodian, and Yangjizhai formations (Li et al., 2006). The Ganquan formation mainly consists of a yellowish conglomerate interbedded with brown-reddish siltstone and sandstone, which can be interpreted as an alluvial fan or braided fluvial deposits. The Yaodian formation is composed of interbedded gray-green marlite and reddish-brown mudstone, known as "Zebra Beds" due to its rhythmic alternation in color. It is analogous to the stratum found in the Linxia Basin in the western Longzhong Basin (Li et al., 1995), which is interpreted as floodplain and shallow lacustrine deposition. More importantly, abundant mammal fossils, such as the teeth and bone fragments of Equidae (*Hipparion weihoense, Hipparion plocodus*) and Rhinocerotidae (*Acerorhinus fuguensis, Chilotherium habereri, and Chilotherium wimani*), were found in the formation, which anchors the temporal framework of the YD section at early Late Miocene (Deng, 2006; Zhang et al., 2011). The Yangjizhai formation is characterized by rhythm cycles composed of reddish-brown mudstone or silty mudstone and yellow–brown calcrete or calcareous. These sediments were interpreted as distal floodplains to palustrine environments (Li et al., 2006). Based on biostratigraphic age control and high-resolution magnetostratigraphy, the Ganquan, Yaodian and Yangjizhai formations range from 12.4 to 11.67 Ma, 11.67 to 7.43 Ma, and 7.43 to 6.40 Ma, respectively (Li et al., 2006; Liu et al., 2016). More details of the depositional environments and chronology have been reported by Li et al. (2006), Alonso-Zarza et al. (2009), and Liu et al. (2016). This study mainly focuses on the late Miocene, as recorded by Yaodian and Yangjizhai formations (~10.83–6.3 Ma).

3.2. Pollen record for the YD section

The palynological record of the YD section consists of 119 samples, with an average temporal resolution of 37 kiloyears (kyr) (Liu et al., 2016). Approximately 65 different palynomorphs were identified at the family or genus level from this section (Supplementary materials). The nearest living relatives of these 65 fossil taxa are mainly distributed in the subtropical, temperate, and warm-temperate humid monsoon climate areas now, such as trees Taxaceae, Hamamelidaceae, Sapindaceae, *Podocarpus*, *Pterocarya*, Rutaceae, *Quercus*, *Ulmus*, Tsuga, *Betula*, *Juglans*, and Cupressaceae, as well as widely distributed shrub and herb species, such as Rosaceae, Poaceae, *Artemisia*, Chenopodiaceae, Asteraceae, and Celastraceae.

Based on the relative changes in abundances of trees, shrubs, and herbs, Liu et al. (2016) concluded that a stepwise aridification of the Asian interior happened at ~ 10.1 Ma and ~ 7–8 Ma, respectively. This succession of vegetation types clearly shows variations in humidity during the period of ~ 10.8–6.4 Ma. This sensitivity of the vegetation to humidity changes allows us to reconstruct the late Miocene precipitation variability at today's the northern boundary of the EASM regime (Li et al., 1988). We refer the readers to Liu et al. (2016) for more detailed information about the pollen record of the YD section.

To investigate the EASM precipitation variations and its driving forces over the orbital timescale, the previously published late Miocene pollen record (~10.83–6.3 Ma, 55 samples) from the YW section (Fig. 1B; Hui et al., 2021) was also integrated into this study.

3.3. The pollen-based climate reconstruction method - CREST

The CREST method is a statistical approach that combines presence-only plant occurrence data with modern climate data to estimate the probability density functions (PDFs) of plant taxa to specific climate variables (Chevalier, 2019; Chevalier et al., 2014). The PDFs represent the statistical relationship between a taxon (e.g. *Betula*) and a specific climate variable (e.g. PWetQ). The method uses a two-step procedure to define the PDFs (Fig. 2). Firstly, parametric PDFs are fitted for each plant species belonging to the pollen taxa (PDF_{sp}). Here, we fitted log-normal PDF_{sp} for PWetQ. Secondly, these species' PDF_{sp} are added with a weight

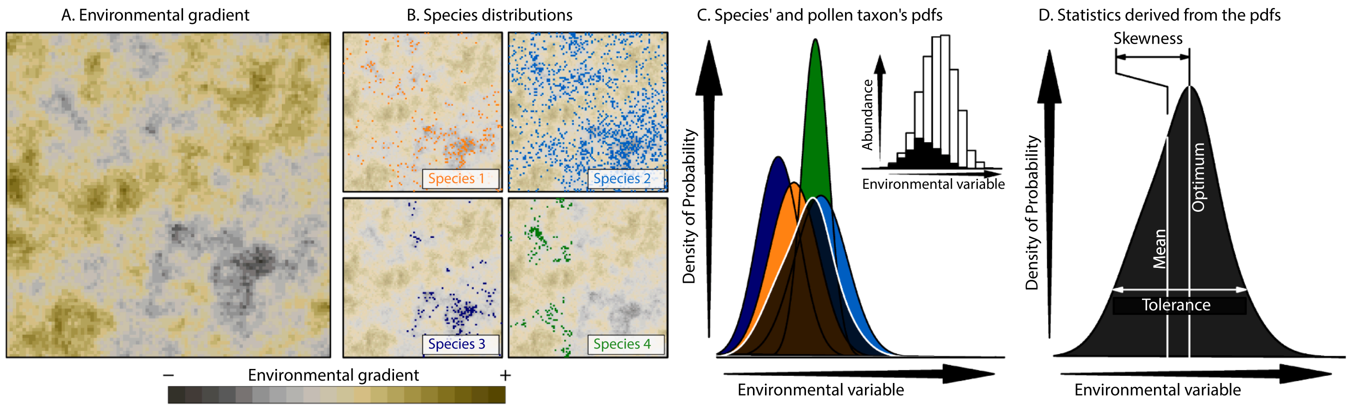

Fig. 2. Conceptual representation of the fitting of probability density functions (pdfs) using randomly generated data (after Hui et al., 2021). (A) Modern distribution of the environmental variable of interest. (B) Modern distribution of four species producing pollen grains in the environment. (C) Four curves representing four pdfs of the species represented in B. Inset histogram represents distribution of modern environment (white) that is occupied by at least one of the four species of interest (black), highlighting the preference for lower values. (D) Representation of statistics (optimum, mean, and width/uncertainty) that can be measured from each pdf to infer climate preferences and tolerances.

determined by their geographical extent to estimate the response of the pollen-type as a single unit (PDF_{pol}). In the second step, the shapes of PDF_{pol} are not constrained so that they can be unimodal, multimodal, or skewed. This is a major benefit of CREST over other reconstruction techniques since many plant taxa have bimodal responses in the East Asian summer monsoon region (Sun et al., 1996). Finally, the different PDF_{pol} are weighted by their corresponding pollen type percentage and multiplied with a weighted geometrical mean. The weighted multiplication of the PDF_{pol} results in a likelihood distribution, from which the climate variable and uncertainties can be derived. The resulting curve describes the likelihood of all climate values considering the co-existence of the pollen taxa in specific proportions and ensures the estimated climate value will be in the mutual climate range of the taxa considered (Chevalier et al., 2014; Chevalier, 2022).

Compared with the Coexistence Approach (CoA) that is widely used in deep time/pre-Quaternary studies (Mosbrugger and Utescher, 1997; Hui et al., 2018a and b), CREST considers the pollen taxa's relative abundance, rather than the presence-only pollen occurrences. This significantly improves the precision of climate reconstructions with uncertainty distributions instead of the more basic climate ranges obtained by CoA. The modern analog technique (MAT; Overpeck et al., 1985) and weighted averaging partial least squares (WA-PLS, ter Braak and Juggins,1993), which are widely employed in late Quaternary (Chevalier et al., 2020) and more rarely in pre-Quaternary (Li et al., 2019) studies, are primarily designed to associate modern proxy observation (e.g. modern pollen assemblage) with their "best analog" and estimate the corresponding climate value as the "best climate estimation". In contrast, CREST estimates and weighs all the climate values based on the nearest living relative of the observed fossil pollen data and yields a probabilistic quantification of all the climate values consistent with the studied fossil pollen data, rather than simple "best" climate estimates.

Studies have shown that using all the pollen types observed in the pollen samples to reconstruct climate is not recommended and CREST usually yields more accurate results when a subset of specific climate-sensitive taxa is picked up (Juggins et al., 2015; Chevalier, 2014, 2022; Hui et al., 2021). When taxa with limited sensitivity to the climate variable to reconstruct are included, the results can be biased by the variables that more strongly define the presence of a taxon. Pollen taxa with a low taxonomic resolution can also be problematic. The PDFs of the pollen taxa composed of hundreds of undifferentiated plant species (e.g., Asteraceae, Poaceae and Rosaceae) can be very large, as the species comprising the pollen type can occupy excessively diverse climate ranges. These PDFs are thus climatically non-informative and can even induce a bias when included in reconstructions (Chevalier et al., 2021). To improve the accuracy of the climate reconstructions, we thus used the following taxa for reconstructing the EASM precipitation-PWetQ: *Alnus*, Buxaceae, *Carpinus*, *Castanea*, *Celtis*, *Corylus*, Hamamelidaceae, *Juglans*, *Larix*, Linaceae, Magnoliaceae, Meliaceae, *Pinus*, Podocarpaceae, *Pterocarya*, *Quercus*, Rutaceae, Sapindaceae, *Stellera*, Taxaceae, *Tilia*, *Tsuga*, *Ulmus* and *Urtica*.

Defining a suitable range for the modern calibration dataset to estimate reliable PDFs is another critical step in the reconstruction using the CREST. The definition of a suitable modern calibration dataset depends on many factors, such as the studied time interval, the studied region, and the reconstructed climatic parameter (Chevalier, 2019; Cao et al., 2017). This implies that we can define the modern calibration dataset based on independent knowledge regarding these influencing factors. The mammal fossil records in the Longzhong Basin (e.g., mainly Linxia and Tianshui Basins) show a warm temperate to subtropical climate conditions during late Miocene in this region, which is similar to that of present-today Hubei, Sichuan and Anhui provinces (Zhang et al., 2011; Deng, 2011). Synthesis studies (including palaeobotanical and lithological evidence) have proven that the EASM system has occurred since the early Miocene and exhibited higher intensity than today during late the Miocene in NE TP (Sun and Wang, 2005; Miao et al., 2016). Therefore, we defined a large rectangular region from 25°N to 40°N, 100°E to 135°E as the modern calibration dataset, in which various climate types are present (e.g., subtropical, warm-temperate and temperate and humid, semi-humid and semi-arid climate types; Fig. 1a; Hui et al., 2021). In addition, the composition of the YD and YW pollen record (consisting of warm temperate and subtropical humid monsoon/EASM region plant taxa) also supports the definition of this calibration dataset (Liu et al., 2016; Hui et al., 2011).

3.4. Spectral analysis

To identify potential orbital cycles, the power spectra of reconstructed PWetQ were analyzed using the 2-MultiTaper Method (Thomson, 1982) with conventional red-noise models (Mann & Lees, 1996) used to estimate the mean, 90, 95, and 99 % confidence levels. The continuous wavelet transform was carried out using wavelet analysis (Torrence & Compo, 1998). Based on the above analysis, the expected dominant spectral components (e.g. Milankovitch frequencies including eccentricity, obliquity, and precession cycles) in the PWetQ records were extracted using Gaussian band-pass filtering. All these analyses were carried out with the Acycle v2.2 program (Li et al., 2019).

4. Results

The reconstructed PWetQ from the YD section indicates that its best estimated values mainly vary between ~ 700–350 mm (Fig. 3). Over long term/tectonic time scales, this record can be broadly divided into two periods. During the period of ~ 10.8–7.6 Ma, the PWetQ record shows a slight decrease trend from ~ 600 mm at ~ 10.8 Ma to ~ 520 mm at ~ 7.6 Ma with regular short cycles. From ~ 7.6 to 6.3 Ma, the PWetQ markedly increases from ~ 400 mm to ~ 600 mm with a larger amplitude in short cycles compared to the previous period. The standard deviation of PWetQ records for these two periods (e.g., standard deviation 75.6 mm and 88.5 mm for the period of ~ 10.8–7.6 Ma and ~ 7.6 to 6.3 Ma, respectively) shows a slight increase, also indicating a higher amplitude of changing.

The previously published PWetQ record during the period ~ 10.8–6.3 Ma from the YW section (Fig. 1B; Hui et al., 2011 and 2021) was integrated with the YW's records as one record to investigate the orbital forcing on EASM precipitation variabilities. These two time series were combined based on the following considerations 1) the two sections, YD and YW, are from the same basin and their depositional environments are almost identical, with the YW section that can also be divided into Ganquan, Yaodian and Yangjizhai formations upwards (Li et al., 2006; Peng et al., 2012; Alonso-Zarza et al., 2009); 2) the dating methods of these two sections are same, combining biostratigraphy and high resolution magnetostratigraphy (Li et al., 2006; Zhang et al., 2013a); 3) both components and variation of these two palynological records from these two sections during ~ 10.8–6.3 Ma are similar (Liu et al., 2016; Hui et al., 2011); 4) finally, the quantitative results of EASM precipitation from these two show synchronous changes (Fig. 3), which further confirms this integration is feasible. We thus derive a relatively high temporal resolution of quantitative EASM precipitation records (mean resolution of ~ 25 kyr) during the period of ~ 10.8–6.3 Ma. As such, this record is likely to have recorded orbital cyclicities with a period longer than at least 100 kyr (Weedon, 2003) and enable us to investigate the driving forces of EASM precipitation over orbital timescales.

The power spectrum analysis of the PWetQ time series shows a dominant 410 kyr band signal throughout the studied interval. Other orbital band signals are also present in some intervals, such as 280 kyr and 140 kyr (Fig. 4). Since the significance of these two orbital bands is below or near 90 % (Fig. 4), the following discussion is focused on the 410 kyr band.

5. Discussion

5.1. Definition of the indices of EASM intensity

A clear and unified definition of EASM strength is the basis for the discussion afterward. Unfortunately, there is no generally accepted definition regarding the EASM intensity probably because of the complex space and time structures of the EASM system and the varying study aims different authors used. Up to now, at least 25 EASM indices have been proposed (Wang et al., 2008), which were mainly based on either "wind" or "rainfall" variations to measure the strength of the EASM (Wang and Ding, 2008; Lau et al., 2000). However, compared with the "wind" signal's elusiveness, the "rainfall" signal is more easily preserved and widespread in the geological archives. It thus provides a practical method for reliable monsoonal reconstruction in deep time (Wang, 2009). In addition, higher rainfall is always associated with intensified southeasterly winds (Wang et al., 2008). Rainfall reconstructions can thus be used to estimate the strength of the EASM and, to some extent, also reflect wind strength changes. Here, we use the precipitation during the wettest quarter (e.g. PWetQ) as the index to reconstruct the late Miocene EASM intensity in NE TP because the maximum rainfall values currently occur in summer. It should be noted that some studies have used the MAP to estimate the Miocene EASM intensity (Miao et al., 2016; Ren et al., 2020; Nie et al., 2020). Arguably, these studies are equivalent to ours, since ~ 60–70 % of the yearly precipitation falls in

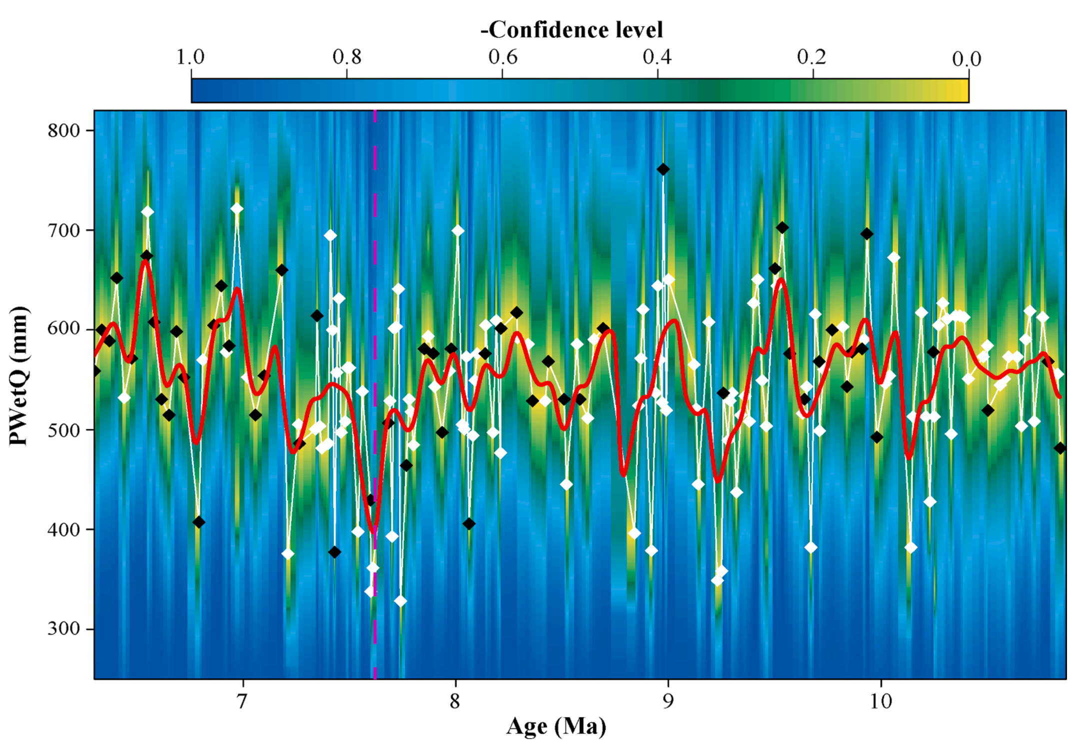

Fig. 3. PWetQ reconstructions from YD and YW sections in Tianshui Basin. White (YD section) and black (YW section) diamonds represent reconstructed values and the red line shows the evenly interpolated values using the Gaussian kernel smoothing approach (Rehfeld et al., 2011). Yellow to blue background color gradient represents uncertainties, here expressed as confidence intervals. Purple vertical lines show the different EASM evolution periods boundaries. (For interpretation of the references to color in this figure legend, the reader is referred to the web version of this article.)

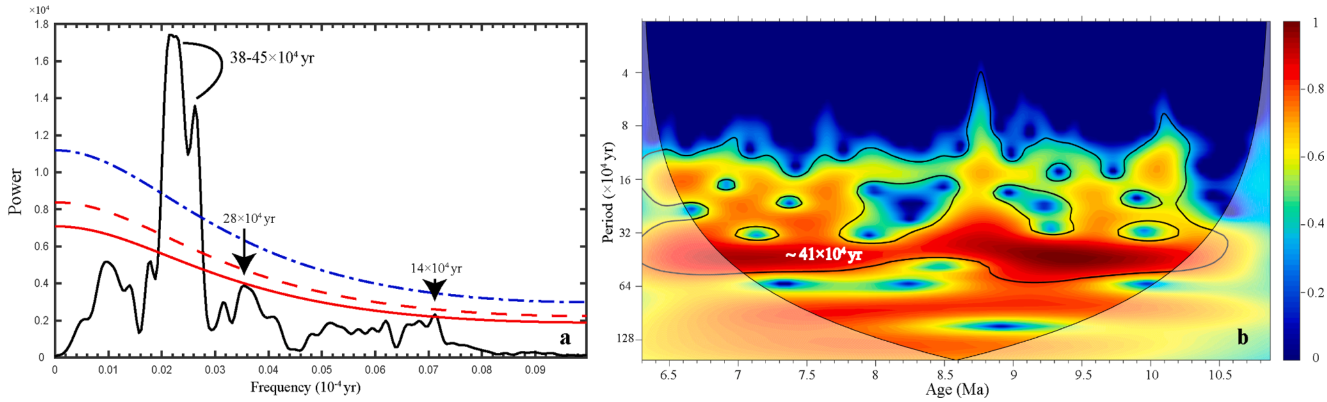

Fig. 4. Spectral analysis of the EASM precipitation during the period of ~ 10.8–6.3 Ma in the Tianshui Basin. (a) Power spectrum for the EASM precipitation, using 2π multitapers method and robust red noise modeling; Dashed blue, dashed red, and solid red lines indicate 99, 95, and 90 % confidence limits, respectively. (b) Wavelet transform of the EASM summer precipitation; The color bars correspond to wavelet power, and the black line denotes a 5 % significance level, the thin black contour shows the "cone of influence". (For interpretation of the references to color in this figure legend, the reader is referred to the web version of this article.)

summers. In other words, changes in PWetQ mainly determine the MAP variations and the reconstructions of EASM intensity based on MAP and PWetQ will have similar trends but different absolute values.

5.2. Mean EASM intensity between ~ 10.8 and 6.3 Ma

The average of the best estimated PWetQ values was ~ 550 mm during the period of ~ 10.8–6.3 Ma in the Tianshui Basin, which is almost 1.8 times as much as today's (~300 mm). This result suggests a humid and subtropical climate (similar to the present-day Xinyang area, southern Henan province in the Huaihe River Basin) prevailed over NE TP during the late Miocene, thus indicating an EASM intensity much stronger than today during the entire ~ 10.8–6.3 Ma interval. This interpretation is supported by many lines of evidence from the NE TP and surrounding areas, although their temporal resolution is very low. These include, for example, the micromorphological characteristics of Miocene palaeosol from the YW section in the Tianshui Basin (Pan et al., 2009), the mammal fossils assemblage from the nearby Linxia Basin (Deng, 2011), the pollen-based MAP reconstructions from the Zeku Basin in north TP (Hui et al., 2018b) and northern China (Miao et al., 2016), the phytolith-based MAP reconstructions from Weihe Basin (Wang et al., 2019a), and the χ_{fd}/HIRM-based MAP reconstructions from the Qaidam Basin (Nie et al., 2020). All these records exhibit much more humid climate conditions during late Miocene than present in NE TP and northern China and thus indicate a stronger late Miocene EASM intensity.

5.3. EASM dynamics from ~ 10.8 to 6.3 Ma

Based on the PWetQ records described in section 4, the detailed evolution process of late Miocene EASM intensity in NE TP can be divided into two distinct stages.

5.3.1. Relatively stable and slight decline of EASM during the period of ~ 10.8–7.6 Ma

During the period of ~ 10.8–7.6 Ma, the best estimated values of PWetQ show a general decreasing trend (e.g., from ~ 600 mm at ~ 10.8 Ma to ~ 520 mm at ~ 7.6 Ma) with a relatively small amplitude (e.g., smaller standard deviation 75.6 mm compared to that of 88.5 mm for the period of ~ 7.6 to 6.3 Ma; Fig. 3 and Supplementary materials) of change in the short cycles, indicating a relatively stable and slight decline of EASM intensity compared to the subsequent period between ~ 7.6–6.3 Ma (Figs. 3 and 5a). This interval corresponds to the typical shallow lacustrine deposition of Yaodian formation, characterized by gray-green marlite and reddish-brown mudstone interbedded, named "Zebra Beds'' due to its regular color oscillations (Li et al., 1995, 2006). The reddish-brown mudstones are interpreted as reflecting a floodplain deposition under oxidizing environment, while the gray-green marlite reflect lacustrine deposition under redox conditions (Li et al., 2006). Overall, the sequence of Yaodian formation reflects a fluvio-lacustrine system with the lake expansions corresponding to the gray-green marlite deposition and the lake contractions corresponding to reddish-brown mudstone (Li et al., 2006; Alonso-Zarza et al., 2009).

The regional hydrological budget in the monsoon region is mainly controlled by the EASM rainfall. The lake level cyclic changes recorded by the lithology in the Tianshui Basin thus likely reflect the EASM rainfall and support the short cycles in PWetQ reconstructions with higher and lower values corresponding to lake expansion and contraction, respectively. Generally speaking, the frequency and the time interval of the lake occurrence recorded by the gray-green marlite in the Yaodian formation become smaller and shorter from the bottom to the top (Li et al., 2006; Liu et al., 2016), suggesting the water available decreases through time and thus a long-term decline in EASM intensity. Therefore, the EASM rainfall changes in the long-term and short cycles during the period of ~ 10.8–7.6 Ma in Tianshui Basin recorded by the PWetQ results are consistent with the lithological character.

Up to now, high-resolution and quantitative late Miocene EASM records in NE TP and surrounding areas are rare. Most existing records have a low temporal resolution and are qualitative indicators of EASM intensity. However, these qualitative records provide important general change trends of the EASM evolution and further support our reconstructions. The integrated records of biomarker proxy of Averaged Chain Length (ACL) from the YD, YW, and Qin'an (QA) sections, the χ_{fd} records from the QA section, and the content of illite and ratios of free iron oxide to total iron oxide (Fe_d/Fe_t) from Zhuanglang (ZL) drilling core in Tianshui Basin similarly show a gradually drying pattern from ~ 10.8 to 7.6 Ma and therefore a decrease in the EASM intensity (Fig. 1b, 5b, d, e and f; Peng et al., 2016; Hao et al., 2008; Sun et al., 2015; Zhao et al., 2020). The relatively high temporal resolution of the (I/S + smectite)/(illite + chlorite) ratio in the Heilinding (HLD) section from the nearby Linxia Basin (the I/S denotes the illite/smectite; Fig. 1b) exhibits low values and a relatively stable trend during the period of ~ 10.8–7.6 Ma compared to the rest of the studied interval (Fig. 5c; Yang et al., 2021), suggesting a relatively low and stable intensity of EASM over this interval, broadly consistent with our PWetQ results.

5.3.2. Strengthening of the EASM from ~ 7.6 to 6.3 Ma

The long-term evolution history of the EASM after ~ 8 Ma is the most controversial issue compared with other intervals of the Neogene EASM history. The qualitative records of CIA, pollen assemblage, and combined planktonic foraminifera Mg/Ca and $\delta^{18}O$ from the EASM precipitation source region - SCS suggest a gradual decline of EASM intensity

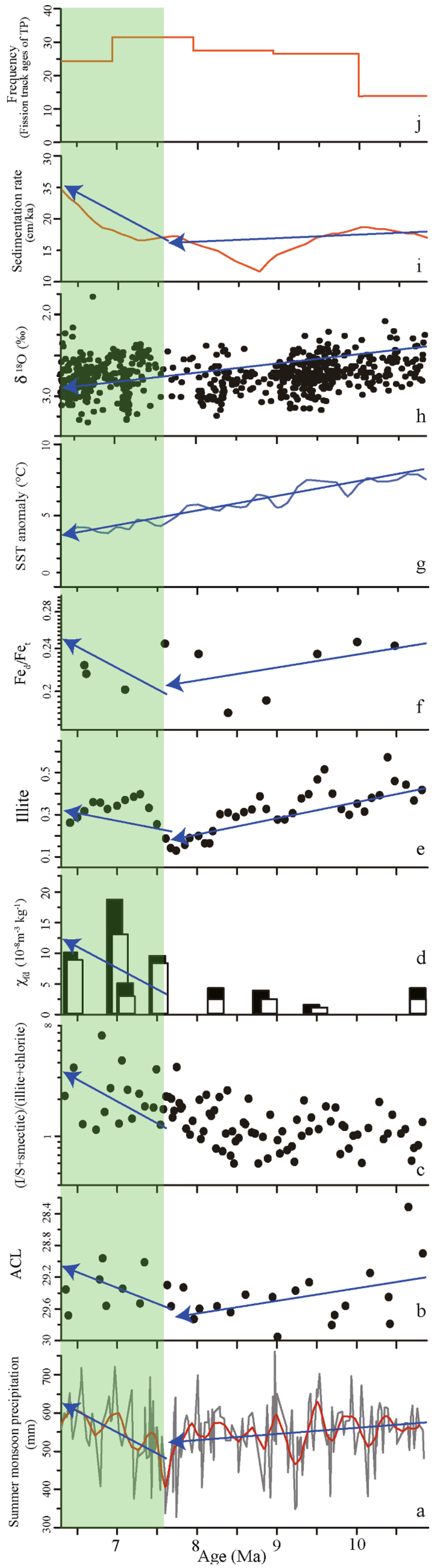

(caption on next column)

Fig. 5. Comparison of reconstructed summer precipitation, with the biomarker, geochemical and magnetic proxy records from the Tianshui Basin, nearby Linxia Basin, and marine and global records from ~ 10.8 to 6.3 Ma. The red lines show the 5-point running average. The blue lines with arrows show the general changing trends, light cyan band highlight the strengthening period. (a) Reconstructed summer precipitation records from the YD and YW sections in Tianshui Basin (this study). (b) Proxy of Averaged Chain Length (ACL) records from the YW, YD and QA sections in the Tianshui Basin (Peng et al., 2016). (c) (I/S + smectite)/(illite + chlorite) ratios from the nearby Linxia Basin (I/S denotes the illite/smectite mixed layer; Yang et al., 2021). (d) The frequency-dependent magnetic susceptibility records from QA section in the Tianshui Basin (Hao et al., 2008). (e-f) The Illite and Fe_d/Fe_t records from the ZL core in the Tianshui Basin (Sun et al., 2015; Zhao et al., 2020). (g) Sea surface temperature (SST) anomalies of North Hemisphere 30°–50°, obtained by subtracting modern SST at this latitude (Herbert et al., 2016). (h) Benthic oxygen isotope record (Zachos et al., 2001). (i) Average sedimentation rate records of the Hexi, Qaidam and Guide Basins on the northeastern TP (Li et al., 2014). (j) Frequency histogram of apatite fission track ages from both the south and north TP (Zhang et al., 2013). (For interpretation of the references to color in this figure legend, the reader is referred to the web version of this article.)

after ~ 8 Ma (Miao et al., 2017; Wan et al., 2010; Steinke et al., 2010). Our quantitative reconstructions show that the EASM intensity exhibits an apparent increasing trend with larger amplitude in short cycles during the period of ~ 7.6–6.3 Ma compared to the previous interval (Figs. 3 and 5a), which is confirmed by the biomarker proxy (Peng et al., 2016), magnetic parameters (Nie et al., 2020; Ren et al., 2020; Hao et al., 2008; Qiang et al., 2011; Ao et al., 2016) and clay minerals records from the NE TP and Chinese loess plateau (Yang et al., 2021).

The vast area of the summer monsoon region and its heterogeneous spatial distribution as well as the ambiguity of monsoon proxy reconstructions, probably led to the conflicting views concerning the long-term EASM evolution after ~ 8 Ma. For example, the detailed Holocene pollen-based EASM precipitation reconstructions from the southern to the northern areas in monsoonal China demonstrate that when the EASM was more intense during the early Holocene (~12000–8000 year BP), summer precipitation increased in southern China, but decreased in the northern area, and vice versa in the late Holocene (~6000–0 year BP). In other words, from southern to northern China, summer precipitation exhibited a mode of spatial variability which can be represented as "+ –" during early Holocene or "– +" during late Holocene (Zhou et al., 2022). This type of spatial distribution of EASM precipitation was also evidenced by the analysis of modern climatological data from the 740 meteorological stations across monsoonal China (Ding et al., 2008). However, determining if there is a dipolar mode of EASM rainfall changes on tectonic timescales during the late Miocene over eastern China requires more high-resolution records from the different regions of monsoonal China.

Regarding the monsoon proxies, a recent study proposes that the temperature is the first-order control on CIA variations at million-year timescales, implying the CIA is probably not a reliable precipitation proxy (Ren et al., 2020). In addition, this strengthening period of EASM intensity from ~ 7.6 to 6.3 Ma recorded by the PWetQ is incompatible with the pollen assemblage records of YW and YD sections in the Tianshui Basin, which show a noticeable drying trend after ~ 7.6 Ma (Hui et al., 2011; Liu et al., 2016). This incompatibility may be attributed to the different pollen species used for quantitative reconstructions and qualitative inferences. Whether a pollen taxon is sensitive to PWetQ or not was assessed using the diagnostics tools embedded in the CREST software before quantitative reconstruction (Chevalier et al., 2014, 2021). The pollen types that were not directly sensitive to PWetQ were excluded from the reconstruction. Generally, the widely distributed plant species were excluded from the reconstruction (also partly because of the low identification resolution of pollen types) since they do not convey specific climate parameter information (such as Poaceae and Rosaceae). The qualitative inference of the drying trend is mainly based on the relative abundance changes of the trees and herbs, that is, higher percentages of trees and lower herbs represent wetter and vice versa (Hui et al., 2011; Liu et al., 2016). However, some trees have more drought-tolerant ability than herbs. For example, some genera in the Cupressaceae (such as *Sabina* and *Juniperus*), which is an important arboreal species for inferring humidity changes in the YD section, are distributed in very arid and cold regions in which herbs cannot survive. Therefore, using these species for inferring humidity changes can bias results. More importantly, it should be noted that these two pollen assemblages were initially interpreted as late to Middle Miocene aridification evolution of interior Asia rather than EASM (Hui et al., 2011; Liu et al., 2016). Therefore, here, we propose that the pollen assemblages of these two sections are composite indicators that may include both the EASM and aridification signal in interior Asia.

It should also be noted that the EASM intensity evolution inferred from the susceptibility and Rb/Sr records from the YD formation only shows orbital cycles (eccentricity) during the late Miocene (Wang et al., 2019b). By contrast, our vegetation (pollen)-based qualitative reconstruction of EASM intensity evolution exhibits not only orbital cycles but also the long-term trend change (Figs. 4, 5a, and 6b). This difference may stem from the different proxies used for reconstructing EASM intensity history. The susceptibility and Rb/Sr results mainly reflect the local (in situ) or smaller region (one lake) precipitation variabilities compared with the pollen assemblages, which are the mixture of large region resources (much beyond one lake) due to is high transporting ability. Thus, the pollen-based monsoonal precipitation has more potential to capture the whole change history of EASM intensity at different time scales. Another possible reason for this difference should be the studied time interval. Former study only informed about the interval of ~ 10–8 Ma and thus did not document the general increasing trend after ~ 8 Ma.

5.4. Possible driving forces of late Miocene EASM evolution

5.4.1. Drivers for the long-term evolution of EASM precipitation

Climate-model simulation studies show that global temperature changes and topography play important roles in the long-term evolution of EASM precipitation during the Neogene (Acosta and Huber, 2020; Farnsworth et al., 2019; Yu et al., 2018). Using low-resolution general circulation model, Farnsworth et al. (2019) explored the drivers for the evolution of the EASM precipitation since the late Cretaceous, and their results suggested that the EASM precipitation increase trend was mainly controlled by the gradual uplift of the Himalayan-Tibetan region since then, with little influence of atmospheric CO_2. By contrast, the results from high-resolution global climate simulations provided by Acosta and Huber (2020) show that the large-scale monsoonal circulations are primarily governed by sea surface temperature (SST) gradients regardless of topography. The topography-Himalayas and Tibet redirect the onshore moisture transport and produce local orographic precipitation that mainly determines the spatial and temporal distribution of monsoonal precipitation. Similarly, a set of sensitivity experiments were conducted using a high-resolution regional climate model to investigate the EASM precipitation variability response to the regional uplift of the TP. The results indicate that the uplift of the TP strengthened both the Indian summer monsoon (ISM) and EASM, whereas the Indian and East Asian winter monsoons showed asynchronous changes in response to the TP uplift (Yu et al., 2018).

Our quantitative reconstruction of EASM precipitation demonstrates that the EASM precipitation gradually decreases from ~ 10.8 to 7.6 Ma, which is broadly parallel to the gradual global cooling during the late Miocene documented by the oxygen isotope and alkenone records (Fig. 5a, g, and h; Zachos et al., 2001; Herbert et al., 2016). Cooler temperatures should reduce the water vapor held in the atmosphere, which can provide additional cooling through the reduced greenhouse effect, and with this positive feedback, further reduce precipitation (Ruddiman, 2002). The late Miocene global cooling and the accompanying development of the east AIS (Zachos et al., 2001) should result in not only sea-level fall and a decline of the source area for water vapor, but also the vast continental shelves at the ocean margins exposed, making it more difficult for the rain belt to reach this inland area (Wang, 1999). Considering that the gradual drying and cooling occurred synchronously, we argue that the decrease in precipitation during the period of ~ 10.8–7.6 Ma was mainly a response to the late Miocene global cooling.

The global temperature decreases continued during the period of ~ 7.6–6.3 Ma. Meanwhile, our reconstructed EASM precipitation markedly increased (Fig. 5a, g, and h; Zachos et al., 2001), suggesting the decoupling of global temperature and regional precipitation during this interval and also implying that global climate is not the sole driving force for the late Miocene EASM variability. As mentioned above, modeling results indicate that changes in the elevation of the TP could have significantly affected the EASM intensity over time. Evidence of sedimentology, paleomagnetism, and thermochronology suggests that an intense uplift of the main body and northeastern TP occurred ~ 8 Ma (Li et al., 2014; Fang et al., 2007; Molnar, 2005). For example, the average sedimentation rate in Hexi, Qaidam, and Guide Basins from northeastern TP rapidly increased since ~ 8 Ma, nearly doubling at ~ 6 Ma (Fig. 5i; Li et al., 2014 and references therein). The palaeomagnetic declination records from the nearby Linxia Basin also indicate a clockwise rotation pattern beginning rapidly after ~ 8 Ma (Fang et al., 2003). Furthermore, the analysis of apatite fission track ages from the whole TP indicates that both the south and north of TP further uplifted at ~ 8 Ma (Fig. 5j; Zhang et al., 2013b).

This synchronicity in the increase in EASM precipitation during the period of ~ 7.6–6.3 Ma seems to coeval with the growth of the TP after ~ 8 Ma. Thus, we suggest that the increased EASM intensity after ~ 7.6 Ma in our records may have been caused by the uplift of the TP after ~ 8 Ma by strengthening the thermal contrast and pressure gradient between land and sea (An et al., 2001; Kutzbach et al., 1989; Wu et al., 2012) and consequently enhanced the water vapor transportation, vapor convergence and ascending movement, as simulated by climate models (Yu et al., 2018). In addition, the intensified EASM intensity caused by the uplift of TP during the late Miocene probably has played a role in global climate cooling (Fig. 5h; Zachos et al., 2001), perhaps through silicate weathering and increased carbon burial (Raymo and Ruddiman, 1992; Yang et al., 2021).

Another notable feature of these two distinct stages is that the mean standard deviations become a little more prominent during the general increase period of ~ 7.6–6.3 Ma (88.5 mm) compared with the previous period of ~ 10.8–7.6 Ma (75.6 mm). This phenomenon is probably related to TP's uplift, which can cause the greatly increased total atmospheric heating (thermal role on precipitation) as demonstrated in the climate simulations provided by Liu et al. (2003), although the detailed mechanism is not clear.

Based on the above analysis, we suggest that, overall long-term evolution of EASM during the late Miocene, global cooling was the dominant factor for the EASM precipitation gradual decrease during the period of ~ 10.8–7.6 Ma in the Tianshui Basin on NE TP. By contrast, the uplift of TP after ~ 8 Ma was the dominant factor for the marked increase in intensity and larger amplitude changes of EASM precipitation during the ~ 7.6–6.3 Ma.

5.4.2. Drivers for the orbital time scale evolution of EASM precipitation

The power spectra and continuous wavelet transform analysis revealed that the quasi-periodicity of ~0.4 Ma is prominent throughout the section, reflecting that monsoonal precipitation in Tianshui Basin variability is mainly paced by eccentricity (Fig. 4a and b; it should be noted that the age model of our EASM precipitation time series does not have any tunning process prior to power spectra and continuous wavelet transform analysis). The monsoon system is mainly present in the middle and low latitudes, where the solar radiation variations are mainly controlled by precession cycles. The precession cycles thus have a significant influence on the summer monsoon precipitation cycles (Liu and

Shi, 2009; Wang, 2009; Ruddiman, 2002). However, the temporal resolution of the monsoon records (such as the EASM precipitation) should be millennial, or even centennial, to investigate the effect of precession on monsoon systems (Wang, 2009). But it is not easy to obtain high-resolution records for pre-Quaternary, especially for the reliable organic proxy records, such as pollen assemblages.

A more suitable approach is to investigate the effect of eccentricity cycles (long-term cycles) on the monsoonal system instead of precession cycles, because the eccentricity influences the monsoonal system by modulating the amplitude of precession (Wang, 2009; Liu and Shi, 2009). Our results indicate that the weak EASM intensity or low precipitation values correspond to eccentricity minima and high precipitation values correspond to maximum (Fig. 6). This is because eccentricity modulates the precession amplitude: the large eccentricity should result in a large amplitude of precession and then lead to a shorter perihelion axis in the Northern Hemisphere (NH) and thus the highest sunshine rate in summer in the NH, finally lead to stronger EASM intensity, and vice versa (Berger and Loutre, 1991; Wang, 2009; Liu and Shi, 2009).

In addition, considering only partial or ephemeral ice existed in the NH during the late Miocene, the dominant eccentricity cycles in the monsoon record can also be linked to insolation-driven AIS orbital periodical (eccentricity) fluctuations (Griener et al., 2015; Patterson et al., 2014; Nie et al. 2017). Because periods of waning and waxing of the AIS could cause periodic changes of SST, eustasy, the position of Intertropical Convergence Zone (ITCZ), intermediate and deep-water production in the Southern Ocean, and amount of latent heat release, which further govern the periodic changes of the ability of the monsoon to transport moisture from the source area to inland of Asia, and finally result in periodical changes of intensity of the EASM in the NE TP (Holbourn et al., 2018; Ao et al., 2021; Nie et al., 2017). For example, during the AIS shrinking scenario, high temperature should strengthen the summer

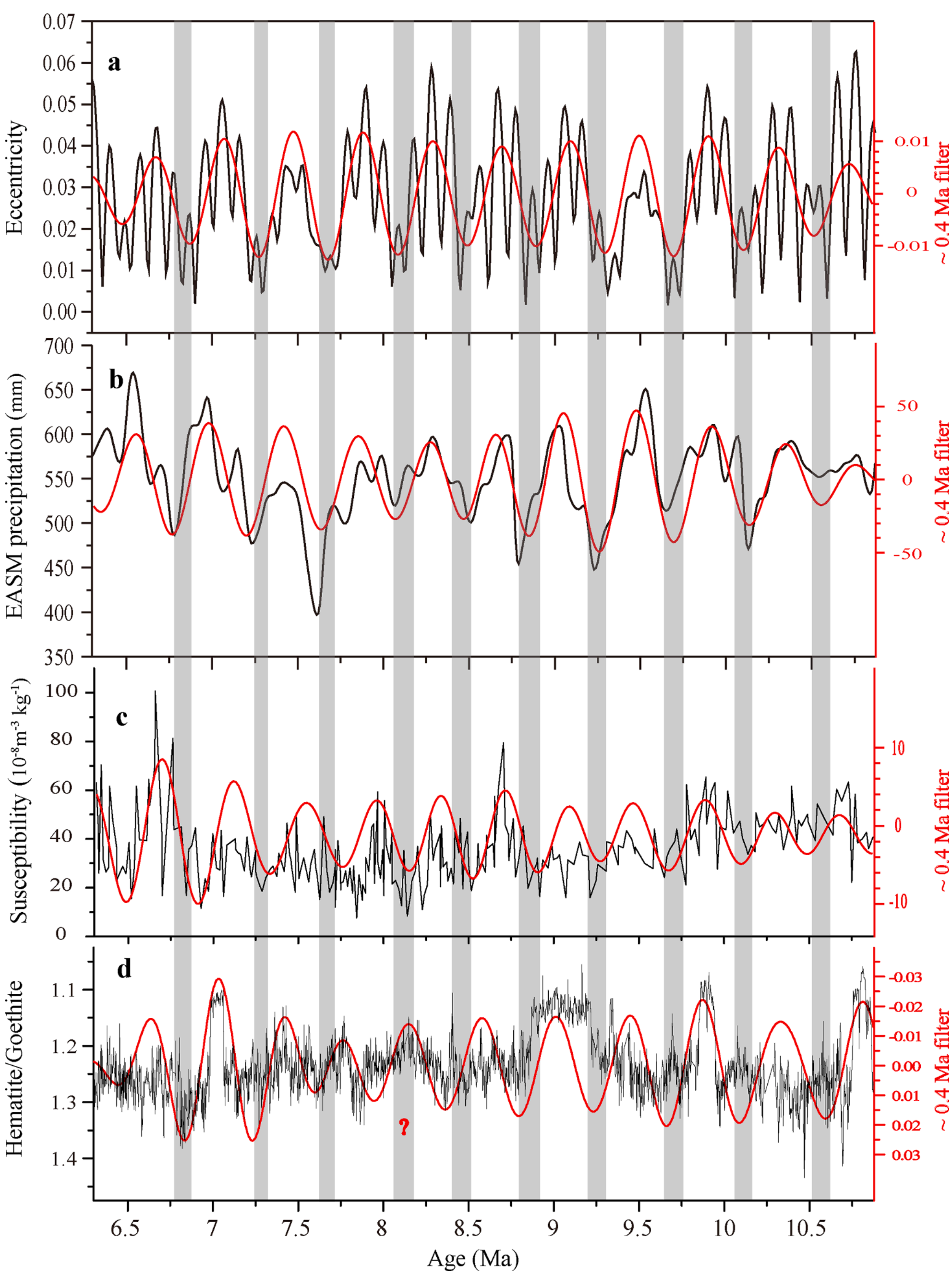

Fig. 6. Spectral analysis of the EASM precipitation record from the Tianshui Basin (this study), and comparison with other EASM records over the interval ~ 10.8–6.3 Ma. (a) Calculated eccentricity (Laskar et al., 2004). (b) EASM precipitation record from the Tianshui Basin (this study). (c) Susceptibility records from the ZL core in Tianshui Basin (Qiang et al., 2011). (d) Hematite/goethite ratios from the ODP Site 1146 in the South China Sea (Holbourn et al., 2021). The red curves in a, b, c and d are their ~ 410 kyr components (centered at frequency 0.00241 with bandwidth 0.0005). (For interpretation of the references to color in this figure legend, the reader is referred to the web version of this article.)

monsoon circulation, increase moisture availability because of latent heat flux, moisture evaporation, and lower-tropospheric water vapor loading increase, shift the ITCZ, summer monsoon rain belt northward and the Pacific Walker Cell westward, shorten the monsoonal moisture transport pathway from the west Pacific Ocean to the Tianshui Basin due to higher sea level, and finally increase the intensity of EASM in the study area (Ao et al., 2021; Nie et al., 2017). This process combined with eccentricity maximum will further increase the precipitation, e.g., amplifying the effect of eccentricity forcing. In contrast, the opposite situation should be occurred during the AIS expansion scenario, as it did during the global cooling period. In addition, numerical simulations have also demonstrated a strong and positive response of northern summer monsoon precipitation to northern summer insolation forcing (Kutzbach et al., 2008). Notably, whether the insolation forcing, the AIS or/and the low-latitude processes dominate the orbital/eccentricity responses of EASM precipitation in the Tianshui Basin, NE TP, they should govern tropical hydrologic variability and subsequently affect the periodic precipitation in this region (Su et al., 2022).

Interestingly, our record is not the only one revealing the eccentricity forcing on the EASM precipitation cycles during the Earth's unipolar icehouse period. Existing studies from different regions indicate that eccentricity-paced Asian summer monsoon variability was a widespread phenomenon (Sun et al., 2022; Ao et al., 2021; Holbourn et al., 2021; Qiang et al., 2011; Wang et al., 2019a, 2020; Nie et al., 2017). For example, the hematite/goethite records from ODP Site 1146 in the monsoonal precipitation source region-South China Sea (Holbourn et al., 2021), grain size records from the fluvial-lacustrine sequence in Weihe Basin in northern China (Wang et al., 2019a), geochemical records from red clay in the Chinese Loess Plateau (Ao et al., 2021) and magnetic parameters from the fluvial-lacustrine sequence in Qaidam Basin (Nie et al., 2017) also exhibit strong eccentricity forcing of Asian summer precipitation during the Miocene.

6. Conclusion

For the first time, we present a relatively high temporal resolution, quantitative and organic proxy-based records of the late Miocene EASM precipitation in NE TP. Overall, the EASM intensity during the period of ~ 10.8–6.3 Ma indicated by the reconstruction of PWetQ values was much stronger than that of today's in the Tianshui Basin, suggesting humid and subtropical climate conditions similar to that of present-day Xinyang area, southern Henan province in the Huaihe River Basin, ~ 950 km to the southeast of Tianshui city. In the long-term trend, the late Miocene EASM precipitation evolution history can be divided into two stages: a relatively stable and slight decline stage during ~ 10.8–7.6 Ma, and followed by a strengthening period from ~ 7.6 to 6.3 Ma. Moreover, the increasing standard deviations for these two stages indicate that the amplitude variation of EASM precipitation increased with time. Comparison analysis between our reconstructions of EASM precipitation and other records revealed that, on the tectonic time scales, the decline stage of EASM during the period of ~ 10.8–7.6 Ma was mainly a response to the global cooling, whereas the significant strengthening stage with larger amplitude of ~ 7.6–6.3 Ma can be attributed to the uplift of TP after ~ 8 Ma. On the orbital time scales, the precipitation time series exhibit a pronounced ~ 0.4 Ma periodicity (eccentricity), with lower (higher) values intervals corresponding to eccentricity minima (maximum). We argue that the synchronous phase of the precipitation and eccentricity time series indicate that the eccentricity forcing exerts a dominant influence on EASM precipitation cycles via its modulation of precessional amplitude, and the period waning and waxing of AIS also probably be another important driving force during that time.

Declaration of Competing Interest

The authors declare that they have no known competing financial interests or personal relationships that could have appeared to influence the work reported in this paper.

Data availability

Data will be made available on request.

Acknowledgement

This work was co-supported by the National Natural Sciences Foundation of China (Grant Nos. 41877445 and 41771209), the Second Tibetan Plateau Scientific Expedition (Grant Nos. 2019QZKK0704) and the State Program of the National Natural Sciences Foundation of China (Grant No. 41330745). Manuel Chevalier was supported by the German Federal Ministry of Education and Research (BMBF) as a Research for Sustainability initiative (FONA; https://www.fona.de/en, last access: 25 June 2022) through the PalMod Phase II project (grant no. FKZ: 01LP1926D). Special thanks to Editor Markus Egli and two anonymous reviewers for their constructive suggestions and valuable comments on this paper.

Appendix A. Supplementary data

Supplementary data to this article can be found online at https://doi.org/10.1016/j.catena.2022.106752.

References

Acosta, R.P., Huber, M., 2020. Competing Topographic Mechanisms for the Summer Indo-Asian Monsoon. Geophys. Res. Lett. 47, e2019GL085112 https://doi.org/10.1029/2019GL085112.

Alonso-Zarza, A.M., Zhao, Z., Song, C.H., Li, J.J., Zhang, J., Martín-Pérez, A., Martín-García, R., Wang, X.X., Zhang, Y., Zhang, M.H., 2009. Mudflat/distal fan and shallow lake sedimentation (upper Vallesian–Turolian) in the Tianshui Basin, Central China: Evidence against the late Miocene eolian loess. Sed. Geol. 222, 42–51. https://doi.org/10.1016/j.sedgeo.2009.03.010.

An, Z., 2000. The history and variability of the East Asian paleomonsoon climate. Quat. Sci. Rev. 19, 171–187. https://doi.org/10.1016/S0277-3791(99)00060-8.

An, Z., Kutzbach, J.E., Prell, W.L., Porter, S.C., 2001. Evolution of Asian monsoons and phased uplift of the Himalaya-Tibetan plateau since late Miocene times. Nature 411, 62–66. https://doi.org/10.1038/35075035.

An, Z., Wu, G., Li, J., Sun, Y., Liu, Y., Zhou, W., Cai, Y., Duan, A., Li, L., Mao, J., Cheng, H., Shi, Z., Tan, L., Yan, H., Hong, A., Chang, H., Feng, J., 2015. Global Monsoon Dynamics and Climate Change. Annu. Rev. Earth Planet. Sci. 43, 29–77. https://doi.org/10.1146/annurev-earth-060313-054623.

Ao, H., Roberts, A.P., Dekkers, M.J., Liu, X., Rohling, E.J., Shi, Z., An, Z., Zhao, X., 2016. Late Miocene-Pliocene Asian monsoon intensification linked to Antarctic ice-sheet growth. Earth Planet. Sci. Lett. 444, 75–87. https://doi.org/10.1016/j.epsl.2016.03.028.

Ao, H., Rohling, E.J., Zhang, R., Roberts, A.P., Holbourn, A.E., Ladant, J.-B., Dupont-Nivet, G., Kuhnt, W., Zhang, P., Wu, F., Dekkers, M.J., Liu, Q., Liu, Z., Xu, Y., Poulsen, C.J., Licht, A., Sun, Q., Chiang, J.C.H., Liu, X., Wu, G., Ma, C., Zhou, W., Jin, Z., Li, X., Li, X., Peng, X., Qiang, X., An, Z., 2021. Global warming-induced Asian hydrological climate transition across the Miocene-Pliocene boundary. Nat. Commun. 12, 6935. https://doi.org/10.1038/s41467-021-27054-5.

Berger, A., Loutre, M.F., 1991. Insolation values for the climate of the last 10 million years. Quat. Sci. Rev. 10, 297–317. https://doi.org/10.1016/0277-3791(91)90033-Q.

Bradshaw, C.D., Lunt, D.J., Flecker, R., Salzmann, U., Pound, M.J., Haywood, A.M., Eronen, J.T., 2012. The relative roles of CO_2 and palaeogeography in determining late Miocene climate: results from a terrestrial model–data comparison. Clim. Past 8, 1257–1285. https://doi.org/10.5194/cp-8-1257-2012.

Cao, X., Tian, F., Telford, R.J., Ni, J., Xu, Q., Chen, F., Liu, X., Stebich, M., Zhao, Y., Herzschuh, U., 2017. Impacts of the spatial extent of pollen-climate calibration-set on the absolute values, range and trends of reconstructed Holocene precipitation. Quat. Sci. Rev. 178, 37–53. https://doi.org/10.1016/j.quascirev.2017.10.030.

Chevalier, M., 2014. CREST (Climate REconstruction SofTware): a probability density function (PDF)-based quantitative climate reconstruction method. Clim. Past 10, 2081–2098. https://doi.org/10.5194/cp-10-2081-2014.

Chevalier, M., 2019. Enabling possibilities to quantify past climate from fossil assemblages at a global scale. Global Planet. Change 175, 27–35. https://doi.org/10.1016/j.gloplacha.2019.01.016.

Chevalier, M., 2022. crestr: an R package to perform probabilistic climate reconstructions from palaeoecological datasets. Clim. Past 18, 821–844. https://doi.org/10.5194/cp-18-821-2022.

Chevalier, M., Davis, B.A.S., Heiri, O., Seppä, H., Chase, B.M., Gajewski, K., Lacourse, T., Telford, R.J., Finsinger, W., Guiot, J., Kühl, N., Maezumi, S.Y., Tipton, J.R., Carter, V.A., Brussel, T., Phelps, L.N., Dawson, A., Zanon, M., Vallé, F., Nolan, C., Mauri, A., de Vernal, A., Izumi, K., Holmström, L., Marsicek, J., Goring, S.J., Sommer, P.S., Chaput, M., Kupriyanov, D., 2020. Pollen-based climate reconstruction techniques for late Quaternary studies. Earth Sci. Rev. 210, 103384 https://doi.org/10.1016/j.earscirev.2020.103384.

Chevalier, M., Chase, B. M., Quick, L. J., Scott, L., 2021. An atlas of southern African pollen types and their climatic affinities, in Quaternary Vegetation Dynamics – The African Pollen Database 35, 239–258, CRC Press, London, https://www.taylorfrancis.com/books/9781003162766/chapters/10.1201/9781003162766-15.

Clift, P.D., 2020. Asian monsoon dynamics and sediment transport in SE Asia. J. Asian Earth Sci. 195, 1–11. https://doi.org/10.1016/j.jseaes.2020.104352.

Clift, P.D., Plumb, R.A., 2008. The Asian Monsoon: Causes, History and Effects. Cambridge University Press, Cambridge.

Clift, P.D., Wan, S., Blusztajn, J., 2014. Reconstructing chemical weathering, physical erosion and monsoon intensity since 25 Ma in the northern South China Sea: A review of competing proxies. Earth-Sci. Rev. 130, 86–102. https://doi.org/10.1016/j.earscirev.2014.01.002.

Deng, T., 2006. Chinese Neogene mammal biochronology. Vertebrate Palasiatic 44, 143–163. https://doi.org/10.1360/aps040120.

Deng, T., 2011. Diversity variations of the late Cenozoic mammals in the Linxia Basin and their response to the climatic and environmental background. Quaternary Sci. 34 (4), 577–588 in Chinese with English abstract.

Ding, Y., Wang, Z., Sun, Y., 2008. Inter-decadal variation of the summer precipitation in East China and its association with decreasing Asian summer monsoon. Part I: Observed evidences. Int. J. Climatol. 28, 1139–1161. https://doi.org/10.1002/joc.1615.

Fang, X., Dupont-Nivet, G., Wang, C., Song, C., Meng, Q., Zhang, W., Nie, J., Zhang, T., Mao, Z., Chen, Y., 2020. Revised chronology of central Tibet uplift (Lunpola Basin). Sci. Adv. 6, eaba7298 https://doi.org/10.1126/sciadv.aba7298.

Fang, X.M., Garzione, C., Voo, R.V.d., Li, J.J., Fan, M.J., 2003. Flexural subsidence by 29 Ma on the NE edge of Tibet from the magnetostratigraphy of Linxia Basin, China. Earth Planet. Sci. Lett. 210, 545-560, 10.1016/S0012-821X(03)00142-0.

Fang, X., Zhang, W., Meng, Q., Gao, J., Wang, X., King, J., Song, C., Dai, S., Miao, Y., 2007. High-resolution magnetostratigraphy of the Neogene Huaitoutala section in the eastern Qaidam Basin on the NE Tibetan Plateau, Qinghai Province, China and its implication on tectonic uplift of the NE Tibetan Plateau. Earth Planet. Sci. Lett. 258, 293–306. https://doi.org/10.1016/j.epsl.2007.03.042.

Farnsworth, A., Lunt, D.J., Robinson, S.A., Valdes, P.J., Roberts, W.H.G., Clift, P.D., Markwick, P., Su, T., Wrobel, N., Bragg, F., Kelland, S.-J., Pancost, R.D., 2019. Past East Asian monsoon evolution controlled by paleogeography, not CO_2. Sci. Adv. 5, eaax1697 https://doi.org/10.1126/sciadv.aax1697.

Griener, K.W., SophieWarny, Askin, R., Actonc, G., 2015. Early to middle Miocene vegetation history of Antarctica supports eccentricity-paced warming intervals during the Antarctic icehouse phase. Global and Planetary Change 127, 67-78, 10.1016/j.gloplacha.2015.01.006.

Hao, Q., Oldfield, F., Bloemendal, J., Guo, Z., 2008. The magnetic properties of loess and paleosol samples from the Chinese Loess Plateau spanning the last 22 million years. Palaeogeogr. Palaeoclimatol. Palaeoecol. 260, 389–404. https://doi.org/10.1016/j.palaeo.2007.11.010.

Heitmann, E., Ji, S., Nie, J., Breecker, D., 2017. Orbitally-paced variations of water availability in the SE Asian Monsoon region following the Miocene Climate Transition. Earth Planet. Sci. Lett. 474, 272–282. https://doi.org/10.1016/j.epsl.2017.06.006.

Herbert, T.D., Lawrence, K.T., Tzanova, A., Peterson, L.C., Caballero-Gill, R., Kelly, C.S., 2016. Late Miocene global cooling and the rise of modern ecosystems. Nat. Geosci. 9, 843–849. https://doi.org/10.1038/ngeo2813.

Holbourn, A.E., Kuhnt, W., Clemens, S.C., Kochhann, K.G.D., Jöhnck, J., Lübbers, J., Andersen, N., 2018. Late Miocene climate cooling and intensification of southeast Asian winter monsoon. Nat. Commun. 9, 1584. https://doi.org/10.1038/s41467-018-03950-1.

Holbourn, A., Kuhnt, W., Clemens, S.C., Heslop, D., 2021. A ~12 Myr Miocene record of East Asian monsoon variability from the South China Sea. Paleoceanogr. Paleoclimatol. 36, e2021PA004267 https://doi.org/10.1029/2021PA004267.

Huang, D. S., 1997. Vegetation of Gansu Province, Science and Technology of Gansu Press, Lanzhou, China (in Chinese).

Hui, Z., Li, J., Xu, Q., Song, C., Zhang, J., Wu, F., Zhao, Z., 2011. Miocene vegetation and climatic changes reconstructed from a sporopollen record of the Tianshui Basin, NE Tibetan Plateau. Palaeogeogr. Palaeoclimatol. Palaeoecol. 308, 373–382. https://doi.org/10.1016/j.palaeo.2011.05.043.

Hui, Z., Li, X., Ma, Z., Xiao, L., Zhang, J., Chang, J., 2018a. Miocene pollen assemblages from the Zeku Basin, northeastern Tibetan Plateau, and their palaeoecological and palaeoaltimetric implications. Palaeogeogr. Palaeoclimatol. Palaeoecol. 511, 419–432. https://doi.org/10.1016/j.palaeo.2018.09.009.

Hui, Z., Zhang, J., Ma, Z., Li, X., Peng, T., Li, J., Wang, B., 2018b. Global warming and rainfall: Lessons from an analysis of Mid-Miocene climate data. Palaeogeogr. Palaeoclimatol. Palaeoecol. 512, 106–117. https://doi.org/10.1016/j.palaeo.2018.10.025.

Hui, Z., Zhou, X., Chevalier, M., Wei, X., Pan, Y., Chen, Y., 2021. Miocene East Asia summer monsoon precipitation variability and its possible driving forces. Palaeogeogr. Palaeoclimatol. Palaeoecol. 581, 110609 https://doi.org/10.1016/j.palaeo.2021.110609.

Juggins, S., Simpson, G.L., Telford, R.J., 2015. Taxon selection using statistical learning techniques to improve transfer function prediction. Holocene 25, 130–136. https://doi.org/10.1177/0959683614556388.

Kutzbach, J.E., Guetter, P.J., Ruddiman, W.F., Prell, W., 1989. The sensitivity of climate to late Cenozoic uplift in Southeast Asia and the American southwest: Numerical experiments. J. Geophys. Res. 94, 18393–18407. https://doi.org/10.1029/JD094iD15p18393.

Kutzbach, J.E., Liu, X., Liu, Z., Chen, G., 2008. Simulation of the evolutionary response of global summer monsoons to orbital forcing over the past 280,000 years. Clim. Dyn. 30, 567–579. https://doi.org/10.1007/s00382-007-0308-z.

Laskar, J., Robutel, P., Joutel, F., Gastineau, M., Correia, A., Levrard, B., 2004. A long-term numerical solution for the insolation quantities of the Earth. A & A 428 (1), 261–285. https://doi.org/10.1051/0004-6361:20041335.

Lau, K.-M., Kim, K.-M., Yang, S., 2000. Dynamical and Boundary Forcing Characteristics of Regional Components of the Asian Summer Monsoon. J. Clim. 13 (14), 2461–2482. https://doi.org/10.1175/1520-0442(2000)013<2461:DABFCO>2.0.CO;2.

Li, J., Fang, X., Wang, J., Zhong, W., Cao, J., Pan, B., Ma, H., Zhu, J. J., Zhou, S. Z., Chen, F., Wang, J., Ma, Y., Zhang, Y., 1995. Uplift of Qinghai-Xizang (Tibet) Plateau and global change, Lanzhou University Press, Lanzhou, China.

Li, J., Zhang, J., Song., C., Zhao, Z., Zhang, Y., Wang, X., Zhang, J., Cui, Q., 2006. Miocene Bahean stratigraphy in the Longzhong Basin, northern central China and its implications in environmental change. Sci. China Series D: Earth Sci. 49 (12), 1270-1279, 10.1007/s11430-006-2057-y.

Li, J., Feng, Z., Tang, L., 1988. Late Quaternary monsoon patterns on the loess plateau of China. Earth Surf. Proc. Land. 13, 125–135. https://doi.org/10.1002/esp.3290130204.

Li, J., Fang, X., Song, C., Pan, B., Ma, Y., Yan, M., 2014. Late Miocene-Quaternary rapid stepwise uplift of the NE Tibetan Plateau and its effects on climatic and environmental changes. Quat. Res. 81, 400–423. https://doi.org/10.1016/j.yqres.2014.01.002.

Li, M.S., Hinnov, L., Kump, L., 2019a. Acycle: Time-series analysis software for paleoclimate research and education. Comput. Geosci. 127, 12–22. https://doi.org/10.1016/j.cageo.2019.02.011.

Li, Y., Zhang, Z., Ding, G., Xu, Q., Wang, Y., Chi, Z., Dong, J., Zhang, L., 2019b. Late Pliocene and early Pleistocene vegetation and climate change revealed by a pollen record from Nihewan Basin, North China. Quaternary Sci. Rev. 222, 105905 https://doi.org/10.1016/j.quascirev.2019.105905.

Liu, X.D., Kutzbach, J.E., Liu, Z., An, Z., Li, L., 2003. The Tibetan Plateau as amplifier of orbital-scale variability of the East Asian monsoon. Geophys. Res. Lett. 30 (16), 1839. https://doi.org/10.1029/2003GL017510.

Liu, J., Li, J., Song, C., Yu, H., Peng, T., Hui, Z., Ye, X., 2016. Palynological evidence for late Miocene stepwise aridification on the northeastern Tibetan Plateau. Clim. Past 12, 1473–1484. https://doi.org/10.5194/cp-12-1473-2016.

Liu, X.D., Shi, Z.G., 2009. Effect of precession on the Asian summer monsoon evolution: A systematic review. Chin. Sci. Bull. 54, 3720–3730. https://doi.org/10.1007/s11434-009-0540-5.

Mann, M.E., Lees, J.M., 1996. Robust estimation of background noise and signal detection in climatic time series. Clim. Change 33 (3), 409–445. https://doi.org/10.1007/Bf00142586.

Miao, Y., Song, C., Fang, X., Meng, Q., Zhang, P., Wu, F., Yan, X., 2016. Late Cenozoic genus Fupingopollenites development and its implications for the Asian summer monsoon evolution. Gondwana Res. 29, 320–333. https://doi.org/10.1016/j.gr.2014.12.007.

Miao, Y., Warny, S., Clift, P.D., Liu, C., Gregory, M., 2017. Evidence of continuous Asian summer monsoon weakening as a response to global cooling over the last 8 Ma. Gondwana Res. 52, 48–58. https://doi.org/10.1016/j.gr.2017.09.003.

Molnar, P., 2005. Mio-Pliocene growth of the Tibetan Plateau and evolution of East Asian climate. Palaeontol. Electronica 8, 1–23.

Mosbrugger, V., Utescher, T., 1997. The coexistence approach - a method for quantitative reconstructions of Tertiary terrestrial palaeoclimate data using plant fossils. Palaeogeogr. Palaeoclimatol. Palaeoecol. 134, 61–86. https://doi.org/10.1016/S0031-0182(96)00154-X.

Nie, J., Garzione, C., Su, Q., Liu, Q., Zhang, R., Heslop, D., Necula, C., Zhang, S., Song, Y., Luo, Z., 2017. Dominant 100,000-year precipitation cyclicity in a late Miocene lake from northeast Tibet. Sci. Adv. 3, e1600762.

Nie, J., Ren, X., Saylor, J.E., Su, Q., Horton, B.K., Bush, M.A., Chen, W., Pfaff, K., 2020. Magnetic polarity stratigraphy, provenance, and paleoclimate analysis of Cenozoic strata in the Qaidam Basin, NE Tibetan Plateau. Geol. Soc. Am. Bull. 132 (1–2), 310–320. https://doi.org/10.1130/B35175.1.

Overpeck, J.T., III, T.W., Prentice, I.C., 1985. Quantitative interpretation of fossil pollen spectra: dissimilarity coefficients and the method of modern analogs. Quaternary Research 23, 87-108, 10.1016/0033-5894(85)90074-2.

Pan, M., Song, C., Li, J., Zhang, J., Zhang, P., Hui, Z., 2009. Micromorphological characteristics of Miocene palaeosol and their paleoenvironment significances in Tianshui. Gansu. Acta Pedologica Sinica 46 (4), 578–585 in Chinese with English abstract.

Patterson, M.O., McKay, R., T. Naish1, C.E., Jimenez-Espejo, F.J., Raymo, M.E., Meyers, S.R., Tauxe, L., Brinkhuis, H., Scientists, I.E., 2014. Orbital forcing of the East Antarctic ice sheet during the Pliocene and Early Pleistocene. Nat. Geosci. 7, 841-847, 10.1038/ngeo2273.

Peng, T., Li, J., Song, C., Zhao, Z., Zhang, J., Hui, Z., King, J.W., 2012. Biomarkers challenge early Miocene loess and inferred Asian desertification. Geophys. Res. Lett. 39, L06702. https://doi.org/10.1029/2012GL050934.

Peng, T., Li, J., Song, C., Guo, B., Liu, J., Zhao, Z., Zhang, J., 2016. An integrated biomarker perspective on Neogene Quaternary climatic evolution in NE Tibetan Plateau: implications for the Asian aridification. Quat. Int. 399, 174–182. https://doi.org/10.1029/2012GL050934.

Piao, J., Chen, W., Wang, L., Pausata, F.S.R., Zhang, Q., 2020. Northward extension of the East Asian summer monsoon during the mid- Holocene. Global Planet. Change 184, 103046. https://doi.org/10.1016/j.gloplacha.2019.103046.

Qiang, X., An, Z., Song, Y., Chang, H., Sun, Y., Liu, W., Ao, H., Dong, J., Fu, C., Wu, F., Lu, F., Cai, Y., Zhou, W., Cao, J., Xu, X., Ai, L., 2011. New eolian red clay sequence on the western Chinese Loess Plateau linked to onset of Asian desertification about 25 Ma ago. Sci. China, Ser. D Earth Sci. 54 (1), 136–141. https://doi.org/10.1007/s11430-010-4126-5.

Raymo, M.E., Ruddiman, W.F., 1992. Tectonic forcing of late Cenozoic climate. Nature 359, 117–122. https://doi.org/10.1038/359117a0.

Rehfeld, K., Marwan, N., Heitzig, J., Kurths, J., 2011. Comparison of correlation analysis techniques for irregularly sampled time series. Nonlinear Processes Geophys. 18, 389–404. https://doi.org/10.5194/npg-18-389-2011.

Ren, X., Nie, J., Saylor, J.E., Wang, X., Liu, F., Horton, B.K., 2020. Temperature control on silicate weathering intensity and evolution of the Neogene East Asian summer monsoon. Geophys. Res. Lett. 47, e2020GL088808 https://doi.org/10.1029/2020GL088808.

Ruddiman, W.F., 2002. Earth's Climate: Past and Future. W.H. Freman and Company, New York.

Steinke, S., Groeneveld, J., Johnstone, H., Rendle-Bühring, R., 2010. East Asian summer monsoon weakening after 7.5 Ma: Evidence from combined planktonic foraminifera Mg/Ca and $\delta^{18}O$ (ODP Site 1146; northern South China Sea). Palaeogeogr. Palaeoclimatol. Palaeoecol. 289, 33–43. https://doi.org/10.1038/ncomms11148.

Su, B., Sun, J., Jin, C.S., 2022. Orbital Forcing of Climatic Changes on the Central Tibetan Plateau Reveals Late Oligocene to Early Miocene South Asian Monsoon Evolution. Geophys. Res. Lett. 49, e2021GL097428 https://doi.org/10.1029/2021GL097428.

Sun, Y., Ma, L., Bloemendal, J., Clemens, S., Qiang, X., An, Z., 2015. Miocene climate change on the Chinese Loess Plateau: Possible links to the growth of the northern Tibetan Plateau and global cooling. Geochem. Geophys. Geosyst. 16, 2097–2108. https://doi.org/10.1002/2015GC005750.

Sun, X., Wang, F., Song, C., 1996. Pollen-climate response surface of selected taxa from Northern China. Sci. China, Ser. D Earth Sci. 26 (5), 431–436 in Chinese.

Sun, X., Wang, P., 2005. How old is the Asian monsoon system?—Palaeobotanical records from China. Palaeogeogr. Palaeoclimatol. Palaeoecol. 222, 181–222. https://doi.org/10.1016/j.palaeo.2005.03.005.

terBraak, C.F., Juggins, S., 1993. Weighted averaging partial least squares regression (WA-PLS): an improved method for reconstructing environmental variables from species assemblages. Hydrobiologia 269, 485–502. https://doi.org/10.1007/978-94-017-3622-0_49.

Thomson, D.J., 1982. Spectrum estimation and harmonic analysis. Proc. IEEE 70 (9), 1055–1096. https://doi.org/10.1109/PROC.1982.12433.

Torrence, C., Compo, G.P., 1998. A practical guide to wavelet analysis. Bull. Am. Meteorol. Soc. 79 (1), 61–78. https://doi.org/10.1175/1520-0477(1998)079<0061:Apgtwa>2.0.Co;2.

Wan, S., Clift, P.D., Li, A., Li, T., Yin, X., 2010. Geochemical records in the South China Sea: implications for East Asian summer monsoon evolution over the last 20 Ma, in Clift, P. D., Tada, R. and Zheng, H. (eds) Monsoon Evolution and Tectonics–Climate Linkage in Asia. Geological Society, London, Special Publications 342, 245–263, 10.1029/2004PA001115.

Wang, P.X., 1999. Response of Western Pacific marginal seas to glacial cycles: paleoceanographic and sedimentological features. Mar. Geol. 156, 5–39. https://doi.org/10.1016/S0025-3227(98)00172-8.

Wang, P.X., 2009. Global monsoon in a geological perspective. Chin. Sci. Bull. 54 (7), 1113–1136. https://doi.org/10.1007/s11434-009-0169-4.

Wang, B., Ding, Q., 2008. Global monsoon: dominant mode of annual variation in the tropics. Dyn. Atmos. Oceans 44, 165–183. https://doi.org/10.1016/j.dynatmoce.2007.05.002.

Wang, Z., Huang, C., Licht, A., Zhang, R., Kemp, D.B., 2019b. Middle to Late Miocene Eccentricity Forcing on Lake Expansion in NE Tibet. Geophys. Res. Lett. 46, 6926–6935. https://doi.org/10.1029/2019GL082283.

Wang, H., Lu, H., Zhao, L., Zhang, H., Lei, F., Wang, Y., 2019a. Asian monsoon rainfall variation during the Pliocene forced by global temperature change. Nat. Commun. 10, 5272. https://doi.org/10.1038/s41467-019-13338-4.

Wang, Y., Lu, H., Wang, K., Wang, Y., Li, Y., Clemens, S., Lv, H., Huang, Z., Wang, H., Hu, X., Lu, F., Zhang, H., 2020. Combined high- and low-latitude forcing of East Asian monsoon precipitation variability in the Pliocene warm period. Sci. Adv. 6, eabc2414 https://doi.org/10.1126/sciadv.abc2414.

Wang, Z., Shen, Y., Licht, A., Huang, C., 2017. Cyclostratigraphy and Magnetostratigraphy of the Middle Miocene Ashigong Formation, Guide Basin, China, and Its Implications for the Paleoclimatic Evolution of NE Tibet. Paleoceanogr. Paleoclimatol. 33, 1066–1085. https://doi.org/10.1029/2018PA003409.

Wang, B., Wu, Z., Li, J., Liu, J., Chang, C.-P., Ding, Y., Wu, G., 2008. How to Measure the Strength of the East Asian Summer Monsoon. J. Clim. 21, 4449–4463. https://doi.org/10.1175/2008JCLI2183.1.

Webster, P.J., Magana, V.O., Palmer, T.N., Shukla, J., Tomas, R.A., Yanai, M., Yasunari, T., 1998. Monsoons: Processes, predictability, and the prospects for prediction. J. Geophys. Res. Oceans 103, 14451–14510. https://doi.org/10.1029/97JC02719.

Weedon, G.P., 2003. Time-Series Analysis and Cyclostratigraphy. Cambridge University Press, Oxford, United Kingdom.

Wei, G., Li, X.-H., Liu, Y., Shao, L., Liang, X., 2006. Geochemical record of chemical weathering and monsoon climate change since the early Miocene in the South China Sea. Paleoceanography 21, PA4214, 10.1029/2006PA001300.

Wen, X., Liu, Z., Wang, S., Cheng, J., Zhu, J., 2016. Correlation and anti-correlation of the East Asian summer and winter monsoons during the last 21000 years. Nat. Commun. 7, 11999. https://doi.org/10.1038/ncomms11999.

Wu, X., An, Z., Wang, S., 1997. Loess and paleomonsoons. Earth Science Frontiers (China University of Geosceiences, Beijing) 4 (1–2), 1–7 in Chinese with English abstract.

Wu, G., Liu, Y., He, B., Bao, Q., Duan, A., Jin, F., 2012. Thermal Controls on the Asian summer monsoon. Sci. Rep. 2, 404. https://doi.org/10.1038/srep00404.

Yang, Y., Ye, C., Galy, A., Fang, X., Xue, Y., Liu, Y., Yang, R., Zhang, R., Han, W., Zhang, W., Ruan, X., 2021. Monsoon-Enhanced Silicate Weathering as a New Atmospheric CO_2 Consumption Mechanism Contributing to Fast Late Miocene Global Cooling. Paleoceanogr. Paleoclimatol. 36, e2020PA004008 https://doi.org/10.1029/2020PA004008.

Yu, E., Zhang, R., Jiang, D., Ramstein, G., Zhang, Z., Sun, J., 2018. High-resolution simulation of Asian monsoon response to regional uplift of the Tibetan Plateau with regional climate model nested with global climate model. Global Planet. Change 169, 24–47. https://doi.org/10.1016/j.gloplacha.2018.07.002.

Zachos, J., Pagani, M., Sloan, L., Thomas, E., Billups, K., 2001. Trends, Rhythms, and Aberrations in Global Climate 65 Ma to present. Science 292, 686–693. https://doi.org/10.1126/science.1059412.

Zhai, Y., Cai, T., 1984. The Tertiary system of Gansu province, in Gansu Geology, pp. 1–40, People's Press of Gansu, Lanzhou, China (in Chinese).

Zhang, J., Xie, G., Li, J., Song, C., Zhao, Z., Wang, X., Hui, Z., 2011. Mammal fossils and ecological environment features of the Neogene from Qin'an area, Gansu Province. Quaternary Sci. 31 (4), 614–621 in Chinese with English abstract.

Zhang, J., Li, J., Song, C., Zhao, Z., Xie, G., Wang, X., Hui, Z., Peng, T., 2013a. Paleomagnetic ages of Miocene fluvio-lacustrine sediments in the Tianshui Basin, western China. J. Asian Earth Sci. 62, 341–348. https://doi.org/10.1016/j.jseaes.2012.10.014.

Zhang, K., Wang, G., Hong, H., Xu, Y., Wang, A., Cao, K., Luo, M., Ji, J., Xiao, G., Lin, X., 2013b. The study of the Cenozoic uplift in the Tibetan Plateau: a review. Geol. Bull. China 32, 1–18 in Chinese with English abstract.

Zhao, H., Qiang, X., Xu, X., Sun, Y., 2020. Iron oxide characteristics of the Chinese loess-red clay sequences and their implications for the evolution of the East Asian summer monsoon since the Late Oligocene. Palaeogeogr. Palaeoclimatol. Palaeoecol. 534, 109604 https://doi.org/10.1016/j.palaeo.2020.109604.

Zhou, X., Zhan, T., Tu, L., Smol, J.P., Jiang, S., Liu, X., Xu, C., Guo, Z., 2022. Monthly insolation linked to the time-transgressive nature of the Holocene East Asian monsoon precipitation maximum. Geology 50 (3), 331–335. https://doi.org/10.1130/G49550.1.